Applied Surface Science 606 (2022) 154983

Contents lists available at ScienceDirect

Applied Surface Science

journal homepage: www.elsevier.com/locate/apsusc

Full Length Article

Identifying the crystal orientation of epitaxially grown MoO_2 nanoflakes on *c*-sapphire

Junjie Jiang [a], Dingbang Yang [a], Yongsong Wang [a], Xiao Guo [a], Madoune Yassine [a], Wenqiang Huang [a], Tao Xu [a], Shanshan Wang [c], Han Huang [a,d,*], Fangping Ouyang [a,b,d,*], Yongli Gao [e]

[a] Hunan Key Laboratory of Nanophotonics and Devices, Hunan Key Laboratory of Super-microstructure and Ultrafast Process, Central South University, School of Physics and Electronics, Changsha, Hunan 410083, PR China
[b] School of Physics and Technology, Xinjiang University, Urumqi 830046, PR China
[c] Science and Technology on Advanced Ceramic Fibers and Composites Laboratory, College of Aerospace Science and Engineering, National University of Defense Technology, Changsha, Hunan 410073, P. R. China
[d] Powder Metallurgy Research Institute, and State Key Laboratory of Powder Metallurgy, Central South University, Changsha, Hunan 410083, PR China
[e] Department of Physics and Astronomy, University of Rochester, Rochester, NY 14627, USA

ARTICLE INFO

Keywords:
MoO_2
C-sapphire
Epitaxial growth
Crystallographic orientation
Growth mechanism

ABSTRACT

Identifying the crystallographic orientations and understanding the growth mechanism of MoO_2 nanocrystals are important for device applications. Here, we investigate the effect of precursor concentrations in chemical vapor deposition on the orientation of MoO_2 nanoflakes with respect to the substrate surface. X-ray diffraction, optical microscopy, (tilted) scanning electron microscopy, high resolution transmission electron microscopy, selected area electron diffraction, and angle-resolved polarized Raman spectroscopy were used to determine the crystal orientations of the nanoflakes and their epitaxial relationship with *c*-sapphire substrates: lying-down MoO_2 nanoflakes for $MoO_2(010)\|$sapphire(0001) and MoO_2 <001>//sapphire<1$\bar{1}$00>, and standing-up ones for $MoO_2(100)\|$sapphire(0001) and MoO_2 <001>$\|$sapphire<1$\bar{1}$00>. Tentative atomic epitaxial models are proposed to explain the orientation and alignment. The investigations also demonstrated that angle-resolved polarized Raman spectroscopy is a quick and nondestructive method to identify the crystallographic orientations of nanoflakes.

1. Introduction

Transition-metal oxides (TMOs) have been extensively studied for their excellent properties and wide-range applications [1–3]. For instance, molybdenum oxides (MoO_x, with $2 < x < 3$) exhibit compositional and structural diversity due to the multivalent molybdenum, resulting in rich physiochemical properties and gathering much research attention recently [4,5]. Among them, molybdenum trioxide (MoO_3) and dioxide (MoO_2) are of greater interest. While MoO_3 is an n-type semiconductor with a wide bandgap of 3.1 eV [6], MoO_2 is metallic with a high melting point and chemical stability [7–9]. Structurally, both are consisting of point- and edge-sharing distorted MoO_6 octahedra but in different ways [10]. Different from the most thermostable layered MoO_3 (α-MoO_3) in orthogonal phase, non-layered MoO_2 is in monoclinic rutile structure (m-MoO_2) with a space group P21/c and its lattice parameters are $a = 0.561$ nm, $b = 0.486$ nm, $c = 0.562$ nm, $\alpha = \gamma = 90°$, and $\beta = 120.93°$ (152316-ICSD). Such low symmetry makes m-MoO_2 highly anisotropic in electrical and optical properties [9].

In the past decades, m-MoO_2 in different morphologies has been synthesized on various substrates [11–13]. MoO_2 thin films can van der Waals epitaxially grow on mica with a crystalline relationship of the surface normal $MoO_2(010)\|$muscovite(001) and the crystal direction MoO_2 <001>$\|$muscovite <100> for flexible and transparent electronic devices [12]. MoO_2 nanorods can epitaxially grow on *c*-sapphire along sapphire<1$\bar{1}$00> with (100), (110) and (1$\bar{1}$0) planes exposed and trapezoidal cross-section as well as on *m*-sapphire along the sapphire <0001> with exposed (100) and (001) planes and triangular cross-sections [7,8]. Well-crystallized MoO_2 nanoflakes can randomly grow

* Corresponding authors at: Hunan Key Laboratory of Nanophotonics and Devices, Hunan Key Laboratory of Super-microstructure and Ultrafast Process, Central South University, School of Physics and Electronics, Changsha, Hunan 410083, PR China.
E-mail addresses: physhh@csu.edu.cn (H. Huang), ouyangfp06@tsinghua.org.cn (F. Ouyang).

https://doi.org/10.1016/j.apsusc.2022.154983
Received 7 August 2022; Received in revised form 12 September 2022; Accepted 18 September 2022
Available online 22 September 2022
0169-4332/

on SiO_2/Si, which display great thermal stability and highly anisotropic electrical conductivity ($\sigma_{max}/\sigma_{min}$ up to 10.1) [9,14,15]. The morphological diversities make MoO_2 promising for various applications in the fields of catalysis, energy storage, and battery anode materials, and as growth templates for transition metal dichalcogenides (TMDCs) [13,16–20]. However, the reported MoO_2 crystal orientations are contradictory. For similar high resolution transmission electron microscope (HR-TEM) and selected area electron diffraction (SAED) results, different crystal planes like MoO_2(1 0 0) [13,19], MoO_2(0 1 0) [9,21], and MoO_2(1 0 1) [20,22] have been identified, which may be attributed to the close lattice parameters (the interlayer distances for (1 0 0), (0 1 0) and (0 0 1) are all about 0.480 nm). Understanding the growth behaviors of MoO_2 and correctly determining their crystal orientations are fundamental and important for its applications in the fields such as catalysis and electronic devices.

In this article, we demonstrate the morphologic competition in nanostructured MoO_2 epitaxially grown on the (0001) surface of crystalline sapphire (*c*-sapphire) depending on the precursor concentrations during chemical vapor deposition (CVD). Optical microscopy (OM), X-ray diffraction (XRD), scanning electron microscopy (SEM) and TEM were used to determine the morphologies and crystal orientations of as-grown MoO_2 nanoflakes. We determined the possible epitaxial relationships between MoO_2 and *c*-sapphire at atomic level and elucidated their growth mechanisms by using growth kinetics. Angle-resolved polarized Raman spectroscopy (ARPRS) was used to confirm the in-plane crystal orientation of MoO_2 nanoflakes quickly and non-destructively.

2. Experiment details

2.1. Growth method

The *c*-sapphire substrates were carefully washed by sequential sonication in acetone, isopropanol, and deionized water, for 10 min per step and two cycles, and dried with nitrogen. Afterward, the samples were mounted on top of a quartz boat located in the right zone by using two SiO_2/Si substrates (with SiO_2 thickness of 300 nm.) supported (as shown in Fig. 1(a)) and facing downwards on top of high-purity MoO_3 powder (15 mg, 99.95%, Aladdin). Another quartz boat containing S powder (300 mg, 99.999%, Aladdin) was placed in the left zone. After that, the quartz tube was flushed with 1200 standard cubic centimeter per minute (s.c.c.m) of nitrogen for 30 min to remove the air. During the growth process, under a flow rate of 300 s.c.c.m of N_2, the temperature in the right zone was raised to 300 °C at a rate of 15 °C/min and held for 30 min, then raised to 780 °C at a rate of 14 °C/min under a flow rate of 25 s.c.c.m and maintained for 10 min. Finally, it was cooled to 550 °C at a rate of 20 °C/min, followed by a natural cooling process. The temperature of the left temperature zone was kept at 50 °C until the end of the synthesis process.

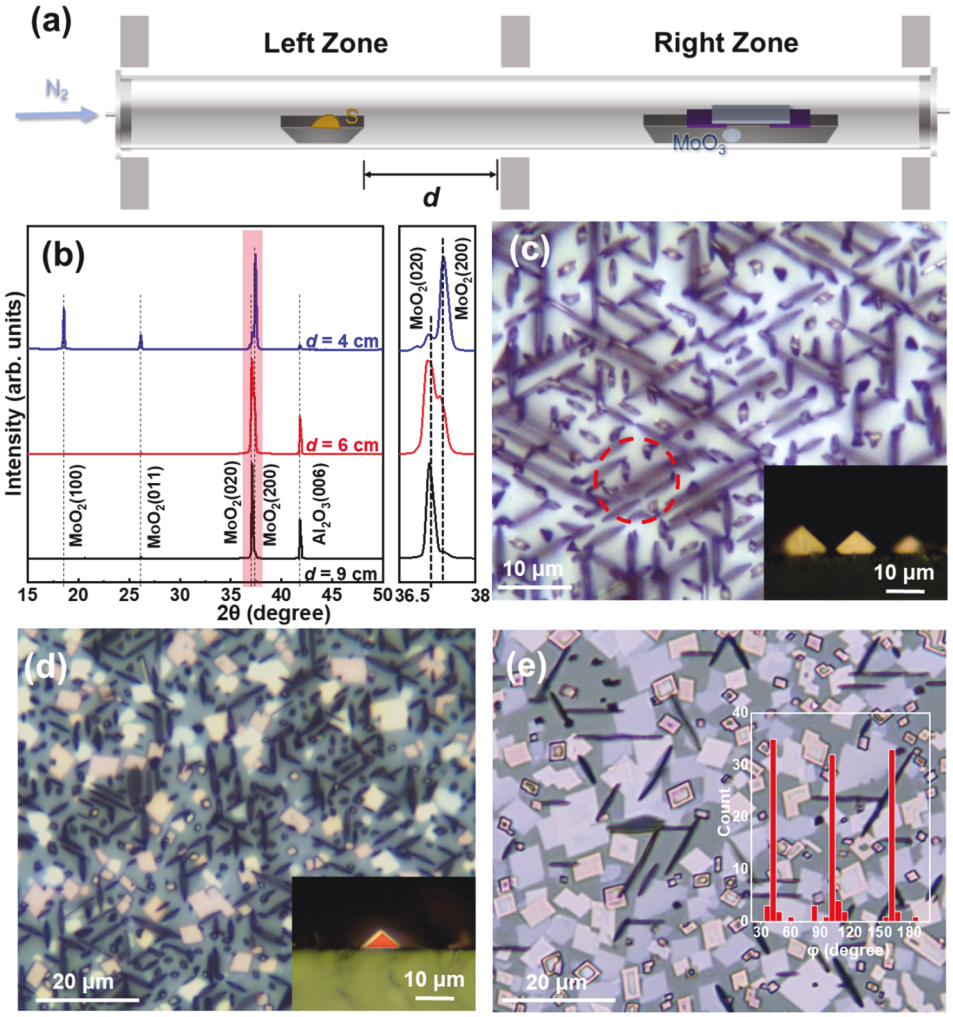

Fig. 1. (a) Illustration of the CVD growth of MoO_2 on *c*-sapphire. (b) Typical XRD patterns of as-grown MoO_2 with different precursor concentrations (different *d*). OM image for $d = 4$ cm (c, inset: cross-sectional OM image), $d = 6$ cm (d, inset: cross-sectional OM image) and $d = 9$ cm (e, inset: orientation histograms for lying-down nanoflakes).

2.2. Sample preparation

The MoO_2-grown c-sapphire was placed backside up on tin foil and cut with a diamond cutter along the sapphire[$1\bar{1}00$] direction to expose the sapphire($11\bar{2}0$) at the edge. A TEM grid was placed backside up on the MoO_2-grown c-sapphire. Slightly sliding the TEM grid, the MoO_2 was transferred to the TEM grid for TEM measurements.

2.3. Characterization

The XRD patterns were collected with Bruker D8 Advance diffractometer. SEM observations were performed on field-emission scanning electron microscopy (Tescan Mira3 LMU) after gold-spray treatment. TEM images and SAED patterns were obtained using transmission electron microscopy (jeol2100f). Raman spectra were recorded with a Renishaw in an inVia Qontor Raman microscope. Spectroscopy data analysis was conducted using *Jade*, *WiRE* and *Origin* software. Curves were plotted by *Origin* software. Simulated XRD patterns were calculated by *VESTA* ver3.5.7 [23]. Simulated SAED patterns were calculated by *ReciPro* ver4.829 software [24]. The first edge of the two sides of the nanoflake was selected that clipped the acute angle clockwise and the angle between the edge and a nanorod was measured. A total of 120 nanosheets were counted for the orientation histogram.

3. Results and discussions

A two temperature zone furnace was used for growth of MoO_2 (For details, please refer to experiment details). Thermal conduction occurs between the two temperature zones in tube furnaces, resulting in slightly different temperatures at different sites. Therefore, maintaining the other settings, the supply of S depends on the distance from the S source to the right temperature zone (defended as *d*, as shown in Fig. 1 (a)). Fig. 1(b) shows the normalized XRD patterns of the samples when $d = 4$ (blue line),6 (red line), and 9 cm (black line). In addition to the *c*-sapphire-related diffraction peaks located at $\sim 42^\circ$, one intuitive difference among the three XRD patterns is the significantly stronger diffraction peaks at $\sim 18^\circ$ and $\sim 26^\circ$ for the $d = 4$ cm sample. Due to crystal symmetry, the diffraction peak at $\sim 18^\circ$ can only correspond to MoO_2(100) but not MoO_2(010) and MoO_2(001), which is consistent with the simulated diffraction results of the powder in Fig. S1 and Tab. S1. The peak located at $\sim 26^\circ$ is assigned to MoO_2(011). Another significant difference among them is the diffraction peaks around 37°. In the enlarged XRD patterns in the right part of Fig. 1(b), two peaks can be distinguished with changed relative intensities, corresponding to the expected peaks of MoO_2(020), and MoO_2(200). As *d* decreases, the intensity ratio of MoO_2(200) to MoO_2(020) increases, which is self-consistent with the $d = 4$ cm sample having the strongest (100) diffraction peak. Thus, there are two kinds of MoO_2 on *c*-sapphire with MoO_2(010)‖sapphire(0001) or MoO_2(100)‖sapphire(0001), suggesting that the precursor concentration can modulate the growth behaviors of MoO_2.

OM images can visually show the different growth behaviors of the three samples. For $d = 4$ cm sample, MoO_2 crystallized mainly into highly oriented pseudo-one-dimensional (1D) structures in ~ 10 μm length and with an angle of 60° to each other, as shown in the top view in Fig. 1(c). Compared with the MoO_2 nanorods grown on *c*-sapphire [7,25,26], the pseudo-1D structures show a marked defocus, suggesting significant out-of-plane features. The inserted cross-sectional OM image (characterization details as shown in Fig. S2) along sapphire<$11\bar{2}0$> reveals the pentagonal structures in a height of ~ 5 μm, confirming the standing-up growth of MoO_2. For $d = 6$ cm sample, except for some pseudo-1D structures with triangular cross-section (inset in Fig. 1(d)) in dark, there are some lying-down parallelogram-shaped flakes in bright contrast in Fig. 1(d). Fig. 1(e) shows a typical OM image of a sample with $d = 9$ cm, lying-down parallelogram-shaped flakes with lateral dimensions of 3 to 10 μm in various thicknesses dominate. The 1D dark features without significant defocus are previously reported highly oriented MoO_2 nanorods [7,25], as revealed by the followed SEM image in Fig. 2(a). The orientation histogram based on 120 lying-down nanoflakes inserted in Fig. 1(e) reveals the epitaxial growth of lying-down MoO_2 flakes on *c*-sapphire due to the substrate 3-fold symmetry induced 60° separation. Considering above XRD results, the MoO_2 lying-down flakes exhibit the (020) planes, while the standing-up flakes exhibit the (200) planes.

To gain further insights into the orientation relationship between MoO_2 nanoflakes and *c*-sapphire, SEM measurements were performed. Fig. 2(a) shows a typical SEM image of a lying-down MoO_2 nanoflake surrounded by long straight MoO_2 nanorods orienting along sapphire <$1\bar{1}00$> [25]. The lying-down MoO_2 nanoflake has a characteristic acute angle of 83°, whose bisector is parallel to the red dotted lines marked MoO_2 nanorods. Thus, the MoO_2 crystalline direction along the bisector is along sapphire <$1\bar{1}00$>.

In order to directly reveal the morphology of the standing-up MoO_2 nanoflakes, a sample was truncated along sapphire<$1\bar{1}00$> to expose the sapphire ($11\bar{2}0$) surface. Fig. 2(b) shows a cross-sectional SEM image along the sapphire<$11\bar{2}0$>, displaying that the standing-up truncated parallelogram MoO_2 nanoflakes have the same characteristic acute angle of $\sim 83^\circ$. The standing-up MoO_2 crystalline direction along the corresponding bisector is along sapphire<$1\bar{1}00$>, too. Conclusively, both lying-down and standing-up MoO_2 nanoflakes have the same shapes and structures with the acute angle bisector parallel to sapphire<$1\bar{1}00$>.

HR-TEM and SAED were used to investigate the crystallographic structure of MoO_2 nanoflakes. The HR-TEM image in Fig. 2(c) exhibits clear parallel fringes with the spacing of 0.237 nm that might be assigned to the (200), (020) or (002) planes of MoO_2, as discussed above in the introduction. The SAED pattern inserted in Fig. 2(c) displays clear Bragg spots in a rectangular pattern, indicating spacing of 0.286 and 0.479 nm in real space. Geometrically, the SAED patterns for the (100), (010), and (001) planes are similar in rectangles. Considering that the diffraction spots of the (0(2n + 1)0) (with n = 0, ±1, ±2, …) planes disappear due to the existing screw axis along MoO_2 <010>, as shown in the simulated SEAD patterns in Fig. S3, only the one for the (010) plane is consistent with the experimental results. Therefore, the exposed parallelogram surfaces of MoO_2 nanoflakes are the (010) planes, consistent with above XRD results. The bisector (83°) is assigned to MoO_2 <001> and the bisector (97°) is assigned to MoO_2 <201>, in consistence with our previous reports on MoO_2 nanorods on *c*-sapphire [7,25]. The detailed atomic structures of both lying-down and standing-up nanoflakes are shown in Fig. 2(d): the exposed (010) crystal plane in parallelogram shape is enclosed by the (102) and ($30\bar{2}$) crystal planes. The epitaxial relationships between MoO_2 nanoflakes and *c*-sapphire are schematically shown in Fig. 2(e) (standing-up, MoO_2(100)‖sapphire (0001) and MoO_2 <001>‖sapphire<$1\bar{1}00$>) and 2(f) (lying-down, MoO_2(010)‖sapphire(0001) and MoO_2 <001>‖sapphire<$1\bar{1}00$ >).

Tilted (45°) SEM measurements were carried out on $d = 6$ cm sample and new trapezoidal nanoflakes with the bottom side parallel to the sapphire<$1\bar{1}00$ > can be observed as intermediates, as shown in Fig. S4. Fig. 3(a) shows a zoom-in tilted SEM image of such a MoO_2 nanoflake with a base angle of $\sim 32^\circ$. Fig. 3(b) shows a HR-TEM image of a transferred trapezoidal nanoflake (enlarged from the marked area in upper right inset) with a base angle of $\sim 42^\circ$, half of the acute angle of a parallelogram nanoflake. The lattice fringe spacings in Fig. 3(b) are measured to be 0.491 and 0.283 nm, respectively. The corresponding SAED pattern (inset in lower right) is consistent with that of parallelogram nanoflakes. Therefore, the trapezoidal nanoflakes can be considered as partial standing-up nanoflakes and the trapezoidal shape is enclosed by the (100), (102), and ($30\bar{2}$) surfaces, as schematically shown in Fig. 3(c). It can be speculated that the orientation relationships

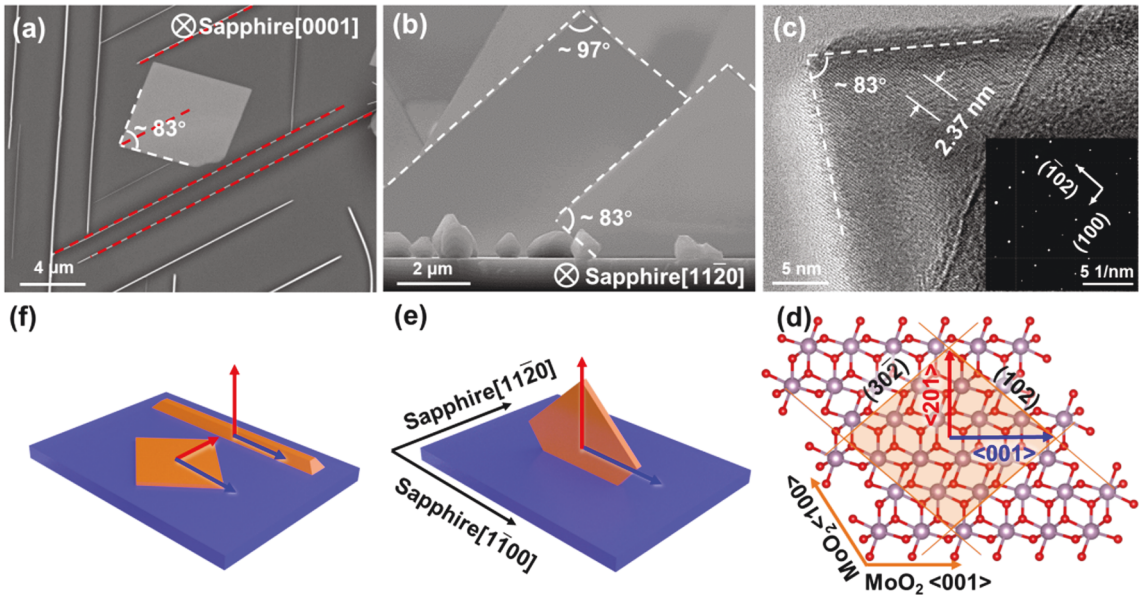

Fig. 2. (a) SEM image of lying-down MoO_2 nanoflakes and nanorods. (b) Cross-sectional SEM image of standing-up MoO_2 nanoflakes along sapphire<11$\bar{2}$0>. (c) HR-TEM image at the 83° corner of a MoO_2 nanoflake. Inset: SAED pattern. (d) The schematic of MoO_2 (0 1 0) (Mo in purple and O in red) and crystallographic configurations of a nanoflake. The proposed models of standing-up (e) and lying-down nanoflakes, nanorods (f).

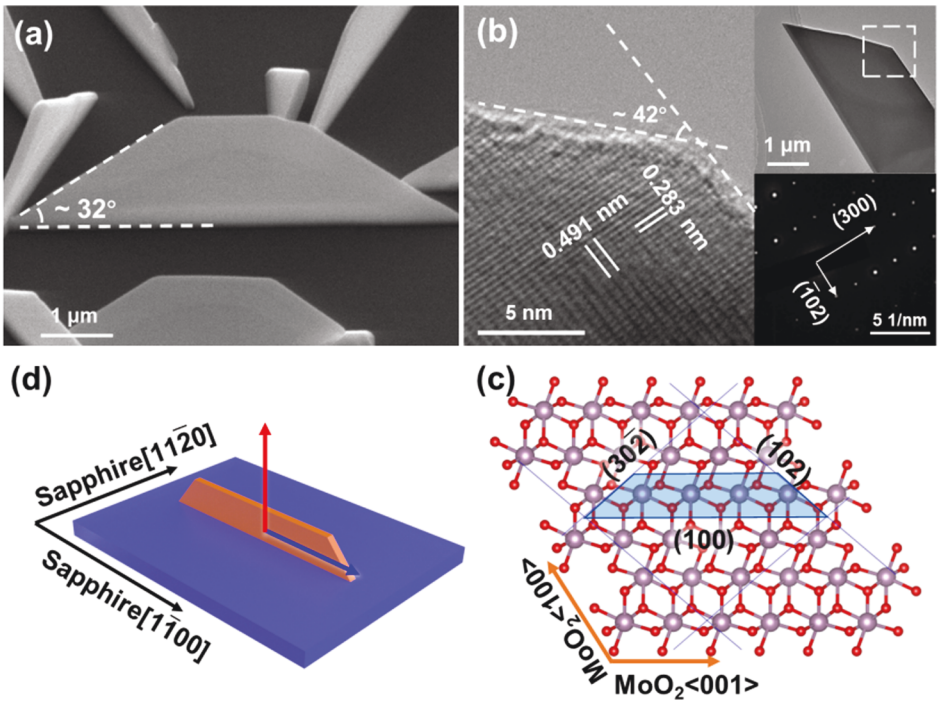

Fig. 3. (a) Tilted (45°) SEM image of standing-up trapezoidal MoO_2 nanoflakes. (b)HR-TEM image of a transferred trapezoidal nanoflake. Insets: low magnification TEM image and SAED pattern. (c) The schematic of trapezoidal nanoflake on MoO_2 (0 1 0). (d) The proposed model of standing-up trapezoidal nanoflake.

of standing-up trapezoidal MoO_2 nanoflakes with the sapphire substrate are MoO_2(1 0 0)‖sapphire(0001) and MoO_2 <0 0 1>‖sapphire<1$\bar{1}$00>, as shown in Fig. 3(d).

The *c*-sapphire exposes the O layer with an in-plane dense stacking structure [27,28]. For metal atoms adsorption on *c*-sapphire, there are usually two preferred adsorption sites: on top of O^1 or in the hollow formed by three nearest-neighbor interfacial O atoms (above Al^1, Al^2, O^2 or Al^3) as shown in the atomic model in Fig. 4(a) and (b) [29,30]. Fig. 4 (c) and (d) show the top and side views of the proposed atomic model of MoO_2 on *c*-sapphire. For lying-down flakes, the O layer of MoO_2(0 1 0) has an in-plane-dense-stacking-like structure interlaced in the same or the reverse direction with *c*-sapphire. The distorted MoO_6 octahedra in MoO_2 flakes are exposed faces in the same direction. Mo atoms at the interface occupy the hollow sites, as shown in Fig. 4(c, left). In contrast, the distorted MoO_6 octahedra in standing-up flakes are exposed corners in the direction perpendicular to the interface. Mo atoms at the interface occupy the top sites, as shown in Fig. 4(c, right). The lattice spacing value of MoO_2 (152316-ICSD) in (0 1 0), (10$\bar{2}$), and (1 0 0) is 0.486, 0.281, and 0.481 nm, respectively. In <11$\bar{2}$0> and <1$\bar{1}$00>, the lattice spacing values of Al_2O_3 (9770-ICSD) are 0.476 and 0.412 nm,

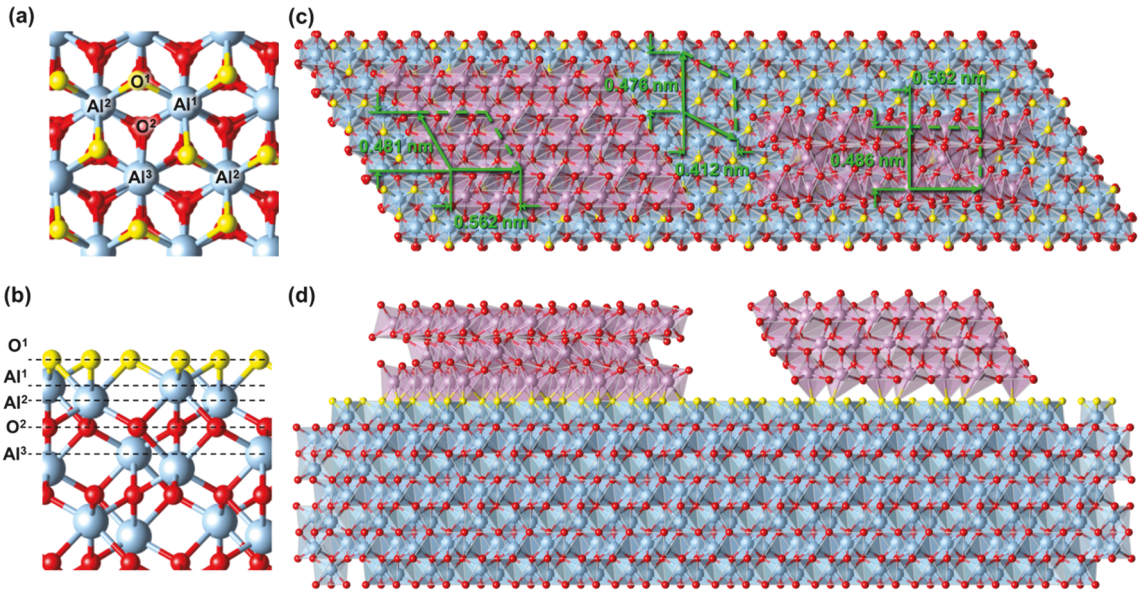

Fig. 4. Top (a) and side (b) views of atomic structure of *c*-sapphire and the commonly considered adsorption sites. (c) Top view of epitaxial relationships between MoO_2 (Mo in purple) and *c*-sapphire (O in red and Al in blue, the interfacial O atoms in yellow) with lying-down growth (left) and standing-up growth (right). (d) Side view.

respectively. The lattice mismatch for lying-down flakes is 2.20% and 1.04% along sapphire<11$\bar{2}$0> and sapphire <1$\bar{1}$00> directions, respectively, while that for standing-up flakes is 2.20% and 2.10% in sapphire<11$\bar{2}$0> and sapphire <1$\bar{1}$00> directions, respectively. Such small lattice mismatches ensure the epitaxial growth of both MoO_2 flakes on *c*-sapphire. The surface energies of MoO_2(100) (7.38 J/m^2), MoO_2(010) (7.45 J/m^2), and MoO_2(001) (7.40 J/m^2) are not significantly different [20], but both lying-down and standing-up MoO_2 nanoflakes exhibit significant growth rate anisotropy. The underlying reason may be that the (010) surface is easily reconstructed to reduce the surface energy [31]. The appearance of in-plane and out-of-plane growth reveals the competition of the epitaxial growth between MoO_2 <201>||sapphire<11$\bar{2}$0> and MoO_2 <010>||sapphire<11$\bar{2}$0>, with the same epitaxy in the sapphire<1$\bar{1}$00> direction. Kinetically, higher precursor concentrations will induce exposure of high surface energy surfaces and overcome larger lattice mismatches, leading to out-

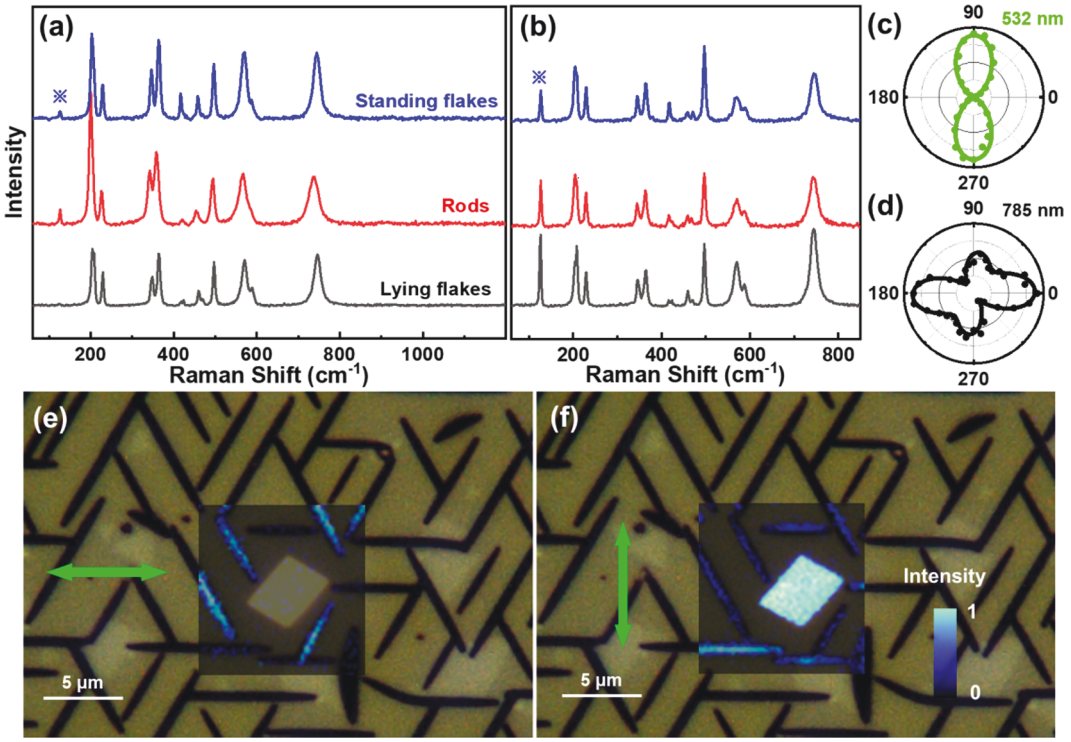

Fig. 5. Normalized Raman spectra (to 228 cm^{-1}) of lying-down nanoflakes (black line), rods (red line), standing-up nanoflakes (characterized from side, blue line) with P_L||(a) and ⊥ (b) sapphire<1$\bar{1}$00> under 532 nm laser. Polar plots of 125 cm^{-1} under 532 nm (c) and 785 nm laser (d). 0° means P_L||sapphire<1$\bar{1}$00>. Raman intensity maps (532 nm) with 40% transparency at 125 cm^{-1} with P_L||(e) and ⊥ (f) sapphire<1$\bar{1}$00> overlapped on the OM image. (P_L: green double arrow).

of-plane growth [32]. More information on the formation mechanisms of MoO_2 in different shapes is discussed in Fig S5. By controlling the precursor concentration at the nucleation stage, the transition between in-plane and out-of-plane growth can be achieved. It should be important to control the two modes of the oxide growth, as it is easy to have traditional gating of devices for the nanoflakes of in-plane growth mode, and more natural to apply gate-all-around (GAA) technology for those of the out-of-plane growth mode.

The anisotropic response of Raman modes to linearly polarized light can be used to quickly determine the crystal orientation without damage [33,34]. Fig. 5(a) shows the Raman spectra with the excitation laser polarization (P_L) parallel to sapphire$<1\bar{1}00>$. In addition to the characteristic peaks of *c*-sapphire at 417, 577, and 751 cm^{-1} [35], the peaks at 125, 203, 208, 228, 347, 364, 423, 459, 469, 497, 571, 589, and 748 cm^{-1} belong to MoO_2, which coincide with previous report [36]. The Raman spectra with $P_L \perp$ sapphire$<1\bar{1}00>$ are shown in Fig. 5(b). The characteristic Raman modes of MoO_3 are not detected [34], confirming the high purity of MoO_2. A_g peak at 125 cm^{-1} has significant intensity change in these spectra. Especially for lying-down MoO_2 nanoflakes, it disappears when $P_L \parallel$ sapphire$<1\bar{1}00>$. Fig. 5(c) show the Raman intensity polar plots of mode at 125 cm^{-1} in parallel configuration, according to the polarization Raman intensity color map shown in Fig. S6, showing a periodicity of 180° with the maximum in MoO_2 $<201>$, consistent with previous report on MoO_2 nanoflakes grown on SiO_2/Si [9]. Therefore, the polarization dependence of Raman intensities of 125 cm^{-1} mode under 532 nm laser can be used to determine the in-plane crystal orientation of MoO_2 nanoflakes quickly and non-destructively. Interestingly, the polar plot mode at 125 cm^{-1} under 785 nm laser exhibits centrosymmetry without axisymmetry, as shown in Fig. 5(d) and Fig. S7, which may can be used to determine the out-of-plane crystal orientation of MoO_2 flakes [37]. Fig. 5(e) and (f) display the same OM image overlapped by the Raman intensity maps with 40% transparency at 125 cm^{-1} under 532 nm laser with $P_L \parallel$(e) and $\perp$ (f) MoO_2 $<010>$. The lying-down MoO_2 flake almost disappears Fig. 5(e), but show a pronounced contrast in Fig. 5(f).

4. Conclusions

In summary, (truncated) parallelogram MoO_2 nanoflakes with the same structural properties have been grown on *c*-sapphire in either lying-down or standing-up modes depending on the precursor concentrations. XRD, SEM, HR-TEM and SAED results reveal that the crystal orientations of such MoO_2 nanoflakes are with the bisector (83°) in MoO_2 $<001>$ and their epitaxial relationship with the substrate. In both cases, MoO_2 $<001>$ prefers to parallel to sapphire$<1\bar{1}00>$. The supersaturation of precursors determines that the MoO_2 nanoflakes grow in either lying-down or standing-up modes. Possible atomic models at the interface for epitaxy are proposed. ARPRS is a nondestructive and quick method to identify the crystal orientations of MoO_2 nanoflakes.

CRediT authorship contribution statement

Junjie Jiang: Conceptualization, Methodology, Formal analysis, Investigation, Data curation, Writing – original draft, Writing – review & editing, Visualization. **Dingbang Yang:** Validation, Formal analysis, Investigation, Data curation, Writing – review & editing, Visualization. **Yongsong Wang:** Formal analysis, Investigation, Visualization, Writing – review & editing. **Xiao Guo:** Formal analysis, Visualization, Writing – review & editing. **Madoune Yassine:** Formal analysis, Writing – review & editing. **Wenqiang Huang:** Formal analysis, Writing – review & editing. **Tao Xu:** Formal analysis, Writing – review & editing. **Shanshan Wang:** Formal analysis, Writing – review & editing. **Han Huang:** Conceptualization, Formal analysis, Investigation, Resources, Data curation, Writing – original draft, Writing – review & editing, Supervision, Project administration, Funding acquisition. **Fangping Ouyang:** Writing – review & editing, Project administration, Funding acquisition. **Yongli Gao:** Writing – review & editing, Project administration.

Declaration of Competing Interest

The authors declare that they have no known competing financial interests or personal relationships that could have appeared to influence the work reported in this paper.

Acknowledgements

This work was financially supported by the National Natural Science Foundation of China (Grants No. 11874427, 52073308, 12164046), the Distinguished Young Scholar Foundation of Hunan Province (Grant No. 2015JJ1020) and the Central South University Research Fund for Shenghua scholars (Grant No. 502033019). This work is carried out in part using computing resources at the High Performance Computing Center of Central South University. Y. Gao acknowledges support from the National Science Foundation, United States (NSF, DMR-1903962)

Appendix A. Supplementary material

Supplementary data to this article can be found online at https://doi.org/10.1016/j.apsusc.2022.154983.

References

[1] C. Ahn, A. Cavalleri, A. Georges, S. Ismail-Beigi, A.J. Millis, J.M. Triscone, Designing and controlling the properties of transition metal oxide quantum materials, Nat. Mater. 20 (2021) 1462–1468, https://doi.org/10.1038/s41563-021-00989-2.
[2] Y. Zhu, X. Liu, S. Jin, H. Chen, W. Lee, M. Liu, Y. Chen, Anionic defect engineering of transition metal oxides for oxygen reduction and evolution reactions, J. Mater. Chem. A. 7 (2019) 5875–5897, https://doi.org/10.1039/c8ta12477a.
[3] J. Meyer, S. Hamwi, M. Kröger, W. Kowalsky, T. Riedl, A. Kahn, Transition metal oxides for organic electronics: energetics, device physics and applications, Adv. Mater. 24 (2012) 5408–5427, https://doi.org/10.1002/adma.201201630.
[4] F. Wang, Z. Pang, L. Lin, S. Fang, Y. Dai, S. Han, Origin of magnetism in undoped MoO_2 studied by first-principles calculations, Phys. Rev. B - Condens. Matter Mater. Phys. 81 (2010) 1–7, https://doi.org/10.1103/PhysRevB.81.134407.
[5] W. Ma, P. Alonso-González, S. Li, A.Y. Nikitin, J. Yuan, J. Martín-Sánchez, J. Taboada-Gutiérrez, I. Amenabar, P. Li, S. Vélez, C. Tollan, Z. Dai, Y. Zhang, S. Sriram, K. Kalantar-Zadeh, S.T. Lee, R. Hillenbrand, Q. Bao, In-plane anisotropic and ultra-low-loss polaritons in a natural van der Waals crystal, Nature. 562 (2018) 557–562, https://doi.org/10.1038/s41586-018-0618-9.
[6] Y. Guo, J. Robertson, Origin of the high work function and high conductivity of MoO_3, Appl. Phys. Lett. 105 (22) (2014) 222110, https://doi.org/10.1063/1.4903538.
[7] Q. Xie, X. Zheng, D.i. Wu, X. Chen, J. Shi, X. Han, X. Zhang, G. Peng, Y. Gao, H. Huang, High electrical conductivity of individual epitaxially grown MoO_2 nanorods, Appl. Phys. Lett. 111 (9) (2017) 093505, https://doi.org/10.1063/1.5001183.
[8] J. Liu, J. Shi, D. Wu, X. Zheng, F. Chen, J. Xiao, Y. Li, F. Song, Y. Gao, H. Huang, Epitaxial growth of $<010>$-oriented MoO_2 nanorods on m-sapphire, Curr. Appl. Phys. 20 (2020) 1130–1135, https://doi.org/10.1016/j.cap.2020.07.015.
[9] Q. Zheng, P. Ren, Y. Peng, W. Zhou, Y. Yin, H. Wu, W. Gong, W. Wang, D. Tang, B. Zou, In-plane anisotropic raman response and electrical conductivity with robust electron-photon and electron-phonon interactions of air stable MoO_2 nanosheets, J. Phys. Chem. Lett. 10 (2019) 2182–2190, https://doi.org/10.1021/acs.jpclett.9b00455.
[10] P.R. Huang, Y. He, C. Cao, Z.H. Lu, Impact of lattice distortion and electron doping on α-MoO_3 electronic structure, Sci. Rep. 4 (2014) 7131, https://doi.org/10.1038/srep07131.
[11] K. Radican, N. Berdunov, I.V. Shvets, Studies of the periodic faceting of epitaxial molybdenum oxide grown on Mo(110), Phys. Rev. B - Condens. Matter Mater. Phys. 77 (2008), 085417, https://doi.org/10.1103/PhysRevB.77.085417.
[12] C.-H. Ma, J.-C. Lin, H.-J. Liu, T.H. Do, Y.-M. Zhu, T.D. Ha, Q. Zhan, J.-Y. Juang, Q. He, E. Arenholz, P.-W. Chiu, Y.-H. Chu, Van der Waals epitaxy of functional MoO_2 film on mica for flexible electronics, Appl. Phys. Lett. 108 (25) (2016) 253104.
[13] J. Xu, D. Ho, Precursor concentration ratio: the key to controllable lateral-to-standing MoO_2 flake transition, Chem. Mater. 33 (2021) 6052–6058, https://doi.org/10.1021/acs.chemmater.1c01472.
[14] J. Luo, H. Chen, J. Wang, F. Xia, X. Huang, Direct growth of 2D MoO_2 single crystal on SiO_2/Si substrate by atmospheric pressure chemical vapor deposition, Mater. Chem. Phys. 251 (2020), 123166, https://doi.org/10.1016/j.matchemphys.2020.123166.

[15] H. Wu, X. Zhou, J. Li, X. Li, B. Li, W. Fei, J. Zhou, J. Yin, W. Guo, Ultrathin molybdenum dioxide nanosheets as uniform and reusable surface-enhanced raman spectroscopy substrates with high sensitivity, Small. 14 (37) (2018) 1802276.
[16] U. Kumar Sen, A. Shaligram, S. Mitra, Intercalation anode material for lithium ion battery based on molybdenum dioxide, ACS Appl. Mater. Interfaces. 6 (2014) 14311–14319, https://doi.org/10.1021/am503605u.
[17] Y. Zhu, X. Ji, S. Cheng, Z.Y. Chern, J. Jia, L. Yang, H. Luo, J. Yu, X. Peng, J. Wang, W. Zhou, M. Liu, Fast energy storage in two-dimensional MoO_2 enabled by uniform oriented tunnels, ACS Nano. 13 (2019) 9091–9099, https://doi.org/10.1021/acsnano.9b03324.
[18] D.i. Wu, D. Qi, J. Liu, Z. Wang, Q. Hao, G. Hong, F. Liu, F. Ouyang, W. Zhang, Growth of centimeter-scale single crystal MoO_3 ribbons for high performance ultraviolet photodetectors, Appl. Phys. Lett. 118 (24) (2021) 243101.
[19] Z.P. Degregorio, Y. Yoo, J.E. Johns, Aligned MoO_2/MoS_2 and MoO_2/$MoTe_2$ freestanding core/shell nanoplates driven by surface interactions, J. Phys. Chem. Lett. 8 (2017) 1631–1636, https://doi.org/10.1021/acs.jpclett.7b00307.
[20] X. Chen, G. Liu, W. Zheng, W. Feng, W. Cao, W. Hu, P.A. Hu, Vertical 2D MoO_2/$MoSe_2$ core-shell nanosheet arrays as high-performance electrocatalysts for hydrogen evolution reaction, Adv. Funct. Mater. 26 (2016) 8537–8544, https://doi.org/10.1002/adfm.201603674.
[21] O. de Melo, V. Torres-Costa, Y. González, A. Ruediger, C. de Melo, J. Ghanbaja, D. Horwat, A. Escobosa, O. Concepción, G. Santana, E. Ramos, Interfacial strain defines the self-organization of epitaxial MoO_2 flakes and porous films on sapphire: experiments and modelling, Appl. Surf. Sci. 514 (2020), 145875, https://doi.org/10.1016/j.apsusc.2020.145875.
[22] S.H. Gaikwad, S.P. Mukherjee, 2D MoO_2/N-doped-carbon nanosheets as SERS tweezers: a non-noble metal reusable substrate for selective organic dye detection, ACS Appl. Nano Mater. 4 (2021) 11611–11624, https://doi.org/10.1021/acsanm.1c02151.
[23] K. Momma, F. Izumi, VESTA 3 for three-dimensional visualization of crystal, volumetric and morphology data, J. Appl. Crystallogr. 44 (2011) 1272–1276, https://doi.org/10.1107/S0021889811038970.
[24] Y. Seto, M. Ohtsuka, ReciPro: free and open-source multipurpose crystallographic software integrating a crystal model database and viewer, diffraction and microscopy simulators, and diffraction data analysis tools, J. Appl. Crystallogr. 55 (2022) 397–410, https://doi.org/10.1107/s1600576722000139.
[25] D. Wu, Y. Yang, P. Zhu, X. Zheng, X. Chen, J. Shi, F. Song, X. Gao, X. Zhang, F. Ouyang, X. Xiong, Y. Gao, H. Huang, Epitaxial growth of highly oriented metallic MoO_2@MoS_2 nanorods on C-sapphire, J. Phys. Chem. C. 122 (2018) 1860–1866, https://doi.org/10.1021/acs.jpcc.7b10666.
[26] F. Chen, J. Liu, X. Zheng, L. Liu, H. Xie, F. Song, Y. Gao, H. Huang, Interfaces between MoOx and MoX_2 (X = S, Se, and Te), Chinese Phys. B. 29 (11) (2020) 116802.
[27] P.S.P. Wei, A.W. Smith, Structure of the (0001) Surface of α-Alumina, J. Vac. Sci. Technol. 9 (1972) 1209–1213, https://doi.org/10.1116/1.1317014.
[28] E.A. Soares, M.A. Van Hove, C.F. Walters, K.F. McCarty, Structure of the (formula presented) surface from low-energy electron diffraction: Al termination and evidence for anomalously large thermal vibrations, Phys. Rev. B - Condens. Matter Mater. Phys. 65 (2002) 1–13, https://doi.org/10.1103/PhysRevB.65.195405.
[29] M.E. McBriarty, D.E. Ellis, Cation synergies affect ammonia adsorption over VOX and (V, W)OX dispersed on α-Al_2O_3 (0001) and α-Fe_2O_3 (0001), Surf. Sci. 651 (2016) 41–50, https://doi.org/10.1016/j.susc.2016.03.015.
[30] L. Xiao, W.F. Schneider, Surface termination effects on metal atom adsorption on α-alumina, Surf. Sci. 602 (2008) 3445–3453, https://doi.org/10.1016/j.susc.2008.08.017.
[31] T. Schroeder, J. Zegenhagen, N. Magg, B. Immaraporn, H.J. Freund, Formation of a faceted MoO_2 epilayer on Mo(1 1 2) studied by XPS, UPS and STM, Surf. Sci. 552 (2004) 85–97, https://doi.org/10.1016/j.susc.2004.01.010.
[32] J. Zhang, G. Du, H. Li, Q. Chen, Q. Kuang, Z. Jiang, Z. Xie, Tailoring the chemical potential of crystal growth units to tune the bulk structure of nanocrystals, Small Methods. 5 (2021) 2000447, https://doi.org/10.1002/smtd.202000447.
[33] Y. Wang, F. Chen, X. Guo, J. Liu, J. Jiang, X. Zheng, Z. Wang, M.M. Al-Makeen, F. Ouyang, Q. Xia, H. Huang, In-plane phonon anisotropy and anharmonicity in exfoliated natural black arsenic, J. Phys. Chem. Lett. 12 (2021) 10753–10760, https://doi.org/10.1021/acs.jpclett.1c03218.
[34] Y. Wang, X. Guo, S. You, J. Jiang, Z. Wang, F. Ouyang, H. Huang, Giant quartic-phonon decay in PVD-grown α-MoO_3 flakes, Nano Res. (2022), https://doi.org/10.1007/s12274-022-4734-3.
[35] P.G. Li, M. Lei, W.H. Tang, Raman and photoluminescence properties of α-Al_2O_3 microcones with hierarchical and repetitive superstructure, Mater. Lett. 64 (2010) 161–163, https://doi.org/10.1016/j.matlet.2009.10.032.
[36] M. Dieterle, G. Mestl, Raman spectroscopy of molybdenum oxides: Part II. Resonance Raman spectroscopic characterization of the molybdenum oxides Mo_4O_{11} and MoO_2, Phys. Chem. Chem. Phys. 4 (2002) 822–826, https://doi.org/10.1039/b107046k.
[37] Y. Choi, K. Kim, S.Y. Lim, J. Kim, J.M. Park, J.H. Kim, Z. Lee, H. Cheong, Complete determination of the crystallographic orientation of ReX_2 (X = S, Se) by polarized Raman spectroscopy, Nanoscale Horiz. 5 (2020) 308–315, https://doi.org/10.1039/c9nh00487d.